The effect of artificial heating on the phase mixing of high frequency Alfvén wave in coronal loops

H. Callingham,[1]★ I. De Moortel,[1,2] P. Pagano[3,4]
[1]School of Mathematics and Statistics, University of St Andrews, St Andrews, Fife KY16 9SS, UK
[2]Rosseland Centre for Solar Physics, University of Oslo, PO Box 1029 Blindern, NO-0315 Oslo, Norway
[3]Dipartimento di Fisica & Chimica, Università di Palermo, Piazza del Parlamento 1, 90134 Palermo, Italy
[4]INAF-Osservatorio Astronomico di Palermo, Piazza del Parlamento 1, 90134 Palermo, Italy

Accepted XXX. Received YYY; in original form ZZZ

ABSTRACT

Phase mixing of Alfvén waves in coronal loops has long been considered a candidate to (partially) address the coronal heating problem. However, it has been argued that some coronal loop models used to study wave heating are not self-consistent, because the heating generated by phase mixing of Alfvén waves may be insufficient to maintain the density structure required for phase mixing. In this paper, we use an artificial background heating profile to create and maintain the transverse density profile, then vary its size to examine its influence on the wave-heating process. Using the Lare2D code, a coronal loop model is created featuring field-aligned thermodynamic equilibrium and a cross-field density profile generated and maintained by an artificial background heating profile. The background heating profile is then reduced or removed, and an Alfvén wave driver is applied simultaneously. We show that phase mixing of Alfvén waves in the shell region can fully offset a small decrease in the background heating profile, and that the thermodynamic feedback is sufficiently large to affect the density profile, broadening the region where efficient heating occurs. When the heating function is removed, a sharp decrease in density occurs, and the system becomes a complex interplay between the dissipated wave energy, reduced energetic losses, and decreased plasma thermal capacity. Heating in the shell region is shown to be sufficient to slow the rate of density decrease, leading to the shell density overtaking the interior density and forming a two-peak cross-field density profile.

Key words: MHD – Sun: atmosphere – Sun: corona – Sun: oscillations

1 INTRODUCTION

The presence of Alfvén waves in the solar atmosphere, first postulated by Alfvén (1942), has long been heralded as a potential source of heating due to their ability to carry large amounts of energy into the corona (Wentzel 1974). MHD wave heating has been extensively studied in the literature, both observationally and through numerical modelling (see reviews by e.g. Parnell & De Moortel 2012; Klimchuk 2015; Arregui 2015; Van Doorsselaere et al. 2020; Srivastava et al. 2021). Modern observational data indicate that a wide spectrum of MHD waves is present in the corona, potentially carrying a significant amount of wave energy into the corona (e.g. De Moortel & Nakariakov 2012; Jess et al. 2016; Hinode Review Team et al. 2019). However, this does not necessarily imply that the energy contained in these waves is dissipated on time and/or length scales that address the coronal heating problem (see e.g. Arregui 2015; Van Doorsselaere et al. 2020). Okamoto et al. (2015) presented direct observational evidence of the dissipation process of MHD waves and subsequent heating, which was corroborated by supplementary numerical simulations in Antolin et al. (2015). Classical wave energy dissipation has long been recognised as too inefficient in coronal plasma due to the large associated length scales. The high Reynolds number of coronal plasma ($\approx 10^{14}$) leads to long heating times, relative to the known coronal cooling timescales. Hence, MHD wave dissipation must be accompanied by a process that reduces the heating timescales to be a viable heating mechanism.

Heyvaerts & Priest (1983) suggested phase mixing of Alfvén waves as a potential mechanism to accelerate dissipation. Phase mixing occurs when Alfvén waves propagate along neighbouring field lines with different Alfvén speeds, becoming increasingly out of phase, which creates smaller cross-field length scales, which in turn increase the efficiency of dissipation. Hence, if an Alfvén speed gradient is present across a loop, waves propagating along the loop from one footpoint to another may phase mix, enhancing any viscous or resistive dissipation. Due to the weak damping assumption and strong phase mixing limit used by Heyvaerts & Priest (1983), phase mixing requires several wavelengths to be present within the coronal domain. Thus, the waves most likely to dissipate rapidly by phase mixing are high frequency waves. The dissipation of phase mixed high frequency waves is known to be highly efficient, but the energy of these waves is easily lost through the TR, both upwards from, and downwards into the chromosphere (see e.g. Hollweg 1984; Berghmans & de Bruyne 1995; De Pontieu et al. 2001).

Computational modelling of the solar atmosphere is highly challenging due to the wide range of temporal and spatial scales involved. In particular, the importance of numerical resolution in the transition

★ E-mail: harry.callingham@gmail.com

region (TR) has been a point of considerable study. Bradshaw & Cargill (2013) found that an under-resolved loop TR can underestimate the peak coronal density by at least a factor of two. To address this problem, several methods have been developed to fully resolve the TR without requiring unreasonably high numerical or temporal resolution. Lionello et al. (2009) and Mikić et al. (2013) proposed modifying the thermal conductivity and the optically thin radiation below a fixed temperature, thereby increasing the associated temperature length scale. This modification broadens the TR while preserving the loop's coronal properties and has been widely used in the literature (see, e.g., Zhou et al. 2021; Howson & De Moortel 2022; Pelouze et al. 2023). In addition to the TR, the complex physical mechanisms in the chromosphere pose additional computational challenges. At lower temperatures, only partial ionisation occurs, and the radiation is optically thick, unlike the optically thin radiation (OTR) in the TR and corona. McMurdo et al. (2023) investigated the phase mixing of high frequency Alfvén waves in a partially ionised plasma within the chromosphere, concluding that, depending on the ionisation degree of the plasma, Cowling diffusion may be sufficiently large to balance radiative losses of the chromosphere. Cargill et al. (2015) suggested an alternative approach, where the chromosphere is simply treated as an isothermal mass reservoir, sufficiently large to be unaffected by any mass flows that occur between the chromosphere and corona.

A common approach to studying the phase mixing of Alfvén waves in coronal loops is to create a model that contains a pre-existing Alfvén speed profile (e.g. Pagano & De Moortel 2017; Prokopyszyn et al. 2019; Pagano & De Moortel 2019, and many earlier studies). This is often achieved by imposing a gradient in the cross-field density and temperature profiles to maintain the pressure balance across the loop. However, this approach does not provide a physical mechanism for the background heating function to be sufficiently large to counterbalance the energetic losses of the optically thin radiation and thermal conduction, so the loop profile is in equilibrium. Cargill et al. (2016) investigated the self-consistency of such models, demonstrating that in the setup presented, the heating by the phase mixing of Alfvén waves was insufficient to sustain the initial density profile required for phase mixing. This was corroborated by Van Damme et al. (2020), which self-consistently explored the thermodynamic feedback associated with high frequency Alfvén wave heating. Despite highly efficient dissipation of the Alfvén waves, the amount of heating generated was multiple orders of magnitude smaller than the imposed background heating profile, implying that wave heating alone is unable to support the required transverse density profile and thus self-consistent wave heating. In addition, although phase mixing has been shown to be a highly effective mechanism for reducing the timescales over which wave heating can occur, it remains an open question whether the associated thermodynamic feedback can alter the density profile on the required timescales. Both Ofman et al. (1998) and Cargill et al. (2016) concluded that the chromospheric evaporation generated by wave heating was insufficient to significantly alter the local density profile within the cooling and draining timescales.

Callingham et al. (2024) expanded the study presented by Van Damme et al. (2020), showing that the dissipation of high frequency Alfvén waves can cause sufficient heating and subsequent thermodynamic feedback to affect the loop density profile. The region where efficient phase mixing could occur was shown to expand towards the exterior of the loop, and a new, hotter equilibrium was maintained against the increased energetic losses by the continual wave dissipation. However, the authors also noted that the energy from wave dissipation was an order of magnitude smaller than the artificial background heating, supporting the conclusion of Cargill et al. (2016) that wave heating may be insufficient to sustain the initially imposed density structure.

In this paper, using the coronal loop model presented in Callingham et al. (2024), we investigate the effect of reducing the artificial background heating profile (H_{bg}), whilst simultaneously driving high frequency Alfvén waves into the coronal domain. This allows us to investigate how both the phase mixing process and the efficacy of wave heating evolve as the coronal density of a loop decreases, which is of particular interest given the transient nature of coronal loops. We explore how the temperature, density, and phase mixing processes evolve due to the viscous dissipation of phase mixed Alfvén waves and the reduction in the background heating profile. The paper is structured as follows. In Section 2, the model is briefly described, with the Alfvén wave driver introduced and the effect of reducing the background heating on the initial equilibrium state of the model, in the absence of any Alfvén waves or wave heating. The results are presented in two sections: first, the background heating profile is reduced to $\mathrm{Sim}_{90\ \%}$ and $\mathrm{Sim}_{50\ \%}$ of its initial value and compared to a reference 100 % H_{bg} simulation (presented in detail in Section 3.1 Callingham et al. 2024). Second, the background heating profile is fully removed, and the effect of phase mixing and wave heating on the collapse of the loop profile is presented. Finally, the discussions and conclusions are presented in Section 4.

2 METHOD

2.1 Coronal Loop Model

Using the same computational setup as in Callingham et al. (2024), a 2.5D numerical model of a coronal loop is created; the loop is anchored in two isothermal chromospheres, acting as a mass reservoir as suggested by Cargill et al. (2015), and an artificially broadened TR, following the method proposed by Lionello et al. (2009) & Mikić et al. (2013). The model includes gravity, optically thin radiation (Klimchuk et al. 2008), thermal conduction (Braginskii 1965), and a transverse background heating profile. As in Callingham et al. (2024), the transverse background heating profile is given by

$$H_{\mathrm{bg}}(x) = \alpha \left(\frac{H_2 + H_1}{2} + \frac{H_2 - H_1}{2} \tanh a(-|x| + b) \right), \tag{1}$$

where $H_1 = 3.6 \times 10^{-6}\,\mathrm{J\ m^{-3}s^{-1}}$, $H_2 = 4H_1$ controls the background heating ratio between the exterior and interior, $a = 5\,\mathrm{Mm}^{-1}$ and $b = 1\,\mathrm{Mm}$ are parameters that determine the steepness and width of the heating function, respectively, and α is the parameter that controls the fraction of the heating function that is applied. Initially, α is set to equal 1, which creates the equilibrium state; Figure 1 shows the background heating function where α is set to 1. The cross-field heating profile establishes a density ratio of $\rho_i/\rho_e = 2.5$ between the interior and exterior at the loop apex, forming a 'shell region' where phase mixing can occur due to transverse density gradients. The red dashed lines in Figure 1 represent the boundaries of the shell regions, where the left and right shell regions are defined as the regions bounded by ($-1.4\mathrm{Mm} \leq x \leq -0.6\mathrm{Mm}$) and ($0.6\ \mathrm{Mm} \leq x \leq 1.4\ \mathrm{Mm}$), respectively. For simplicity, the position of the shell region is assumed not to change, and all calculations referring to a quantity within the shell region use the regions defined by the equilibrium state.

The coordinate system used defines y as the field-aligned direction, x as the cross-field direction, and z as the invariant direction. Periodic boundary conditions are implemented in the x-direction, and zero gradient boundary conditions are applied in y. The numerical domain

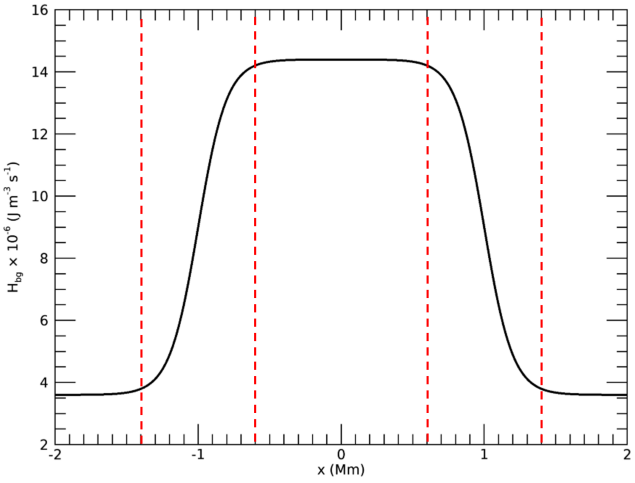

Figure 1. Plot of the background heating profile in the $x-$domain, $H_{\rm bg}(x)$, where $\alpha = 1$. The red dashed lines represent the boundaries of the shell regions (± 1.4Mm $< x < \pm 0.6$Mm).

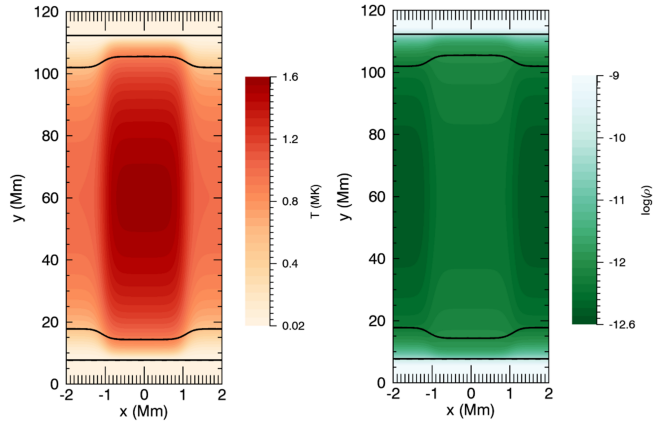

Figure 2. Contour plots of the initial temperature (left) and density (right) profiles after numerical relaxation. The horizontal black lines represent the TR boundaries.

is 4 Mm × 120 Mm, with a grid resolution of 256 × 4096 . The initially uniform magnetic field is set to $B_y = 10$ G and the dynamic viscosity is set to $\rho\nu = 5 \times 10^{-4}$ kg m^{-1} s^{-1}, with zero resistivity to avoid diffusion of the background magnetic field. The viscosity value, which leads to a Reynolds number of 10^{12} inside the loop, is significantly larger than the numerical viscosity present in the model, as shown in Callingham et al. (2024). After numerical relaxation, thermodynamic equilibrium is maintained by a balance between the background heating function, optically thin radiation, and thermal conduction. The initial temperature and density profiles are shown in Figure 2, and the total energy equation of the system is given by:

$$\frac{\partial W}{\partial t} + \nabla \cdot \boldsymbol{F} = H_{\rm bg} - n^2\Lambda(T) - \nabla \cdot \boldsymbol{q} + \rho\nu\nabla^2\boldsymbol{v}, \tag{2}$$

where W denotes the total energy, $\boldsymbol{F}$ the total flux excluding the thermal flux, $H_{\rm bg}$ the background heating function, $n^2\Lambda(T)$ the optically thin radiation, $\nabla \cdot \boldsymbol{q}$ the thermal conduction and $\rho\nu\nabla^2\boldsymbol{v}$ represents the viscous contribution.

2.2 Driver Implementation

The driver is implemented following the same methodology as in Callingham et al. (2024). A continuous, sinusoidal driver is applied to 10 grid points centred around $y = 10$ Mm (i.e., inside the 1st TR) and uniformly across the x domain. The driver is implemented as an additional force in the z-component of the momentum equation:

$$F_z = \rho a_z, \tag{3}$$

$$a_z = -V_0\omega\cos(\omega t), \tag{4}$$

where $\omega = 2\pi/P$ is the angular frequency, $P = 10$ s is the period of the driver and $V_0 = 24.5$ km s^{-1} is a constant, chosen such that the velocity of the resultant waves that propagate in the corona is at the higher end of the observed spectrum. We drive our model through the acceleration a_z to describe the behaviour of the coronal loop footpoints subject to a kinematic high-β driving mechanism. A fixed a_z is chosen instead of a fixed F_z, since keeping the acceleration fixed keeps the velocity constant, mimicking a boundary-driven wave being injected into the domain. The waves propagate upward into the corona and downward toward the chromosphere; the downward waves then reflect off the chromosphere and subsequently propagate upward toward the corona, where they interact with the driven waves. The interference results in Alfvén waves propagating in the corona, with amplitudes at the upper end of the observed range for high frequency waves (McIntosh et al. 2011; Weberg et al. 2018). The Alfvén crossing time ranges from 58 – 99s, with the fastest rate in the loop's exterior and the slowest in its interior. Hence, multiple wavelengths are present in the coronal domain across all of the loop. Within the coronal domain, standing waves form in both the interior and exterior regions, whereas dissipation prevents a standing wave from forming within the shell. For a detailed description of the wave behaviour and associated damping, we refer the reader to Callingham et al. (2024).

2.3 Reducing the Background Heating

In this Paper, the background heating function is reduced by setting α to 0.9 and 0.5, thereby reducing the background heating contribution to 90% and 50% of the equilibrium value, respectively. Henceforth, the two simulations are referred to as the Sim$_{90\ \%}$ and Sim$_{50\ \%}$ cases. The RTV (Rosner-Tucker-Vaiana) scaling laws (Rosner et al. 1978) can be rearranged to estimate how changing the background heating will alter the apex temperature and density:

$$T_2 = \left(\frac{H_{\rm bg,2}}{H_{\rm bg,1}}\right)^{2/7} T_1, \tag{5}$$

$$\rho_2 = \left(\frac{H_{\rm bg,2}}{H_{\rm bg,1}}\right)^{4/7} \rho_1. \tag{6}$$

Here, subscript 1 denotes the initial state and subscript 2 the modified background heating simulation. The scaling laws predict that reducing the background heating function to Sim$_{90\ \%}$ will decrease the loop apex temperature and density to 97% and 94% of their respective original values, and to 82% and 67% in the Sim$_{50\ \%}$ case.

Figure 3 show the cross-field apex temperature, density and Alfén speed gradient profiles after 5200s, for the driven (VD - solid lines) and non-driven (ND - dashed lines) Sim$_{90\ \%}$ and Sim$_{50\ \%}$ cases, represented by the red and blue lines, respectively, in Figures 3, 4 and 7. The top and bottom panels in Figure 4 show the evolution in time of the temperature and density at the loop apex at the edge of the shell

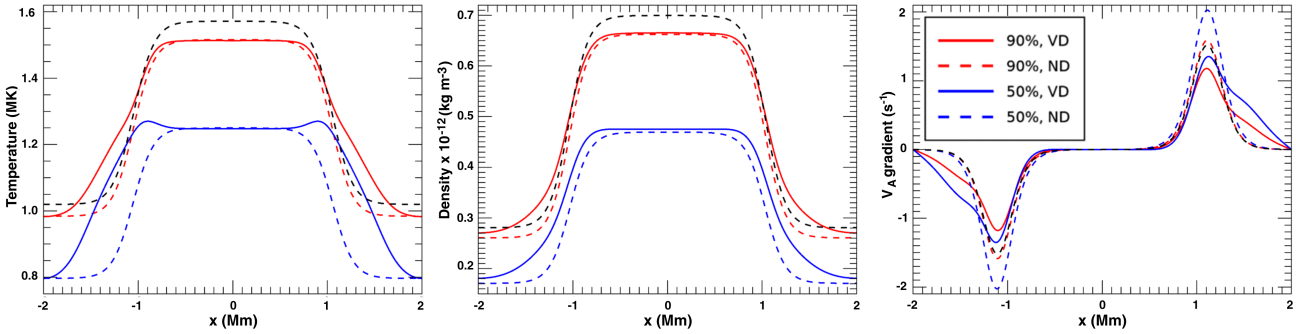

Figure 3. Plot of the temperature (left), density (middle) and cross-field Aflvén speed gradient (right) at the loop apex after 5200s for the driven (solid lines) and non-driven (dashed lines) $\mathrm{Sim}_{90\ \%}$ and $\mathrm{Sim}_{50\ \%}$ cases. The black dashed line represents the initial equilibrium state.

regions ($x = -1.4$Mm, $y = 60$Mm). When the background heating is reduced, the apex temperature in both driven simulations rapidly evolves towards the predicted profile, becoming approximately constant after 800 s in the $\mathrm{Sim}_{90\ \%}$ case and 2200 s in the $\mathrm{Sim}_{50\ \%}$ case. The middle panel of Figure 4 shows the field-aligned velocity, averaged over the 1st TR-coronal boundary in the left-hand shell region as a function of time. The reduction in temperature triggers strong downflows of mass moving from the corona into the TR and chromosphere, resulting in a negative v_y flow across the TR-coronal boundary for both of the non-driven (dashed line) simulations. As expected, stronger downflows occur in the $\mathrm{Sim}_{50\ \%}$ case, with a peak of -2.8 km s^{-1} and moderate downflows remain for the duration of the simulation. Hence, the apex density continually decreases as the system approaches a new equilibrium state. The non-driven simulations approach the predicted values given by the RTV scaling laws (Eq. 5 & 6), but do not reach an equilibrium state within the runtime of the simulation. The colder, less dense loop profiles have lower associated energetic losses, which are balanced by the reduced contribution of the background heating function. In the $\mathrm{Sim}_{50\ \%}$ case, the density decrease is sufficient to reduce the radiation by approximately a factor of two. In addition, the thermal capacity of the plasma decreases linearly with density; therefore, the remaining coronal plasma will be more easily heated. Thus, wave heating may be a more effective heating mechanism in the simulations with decreased background heating.

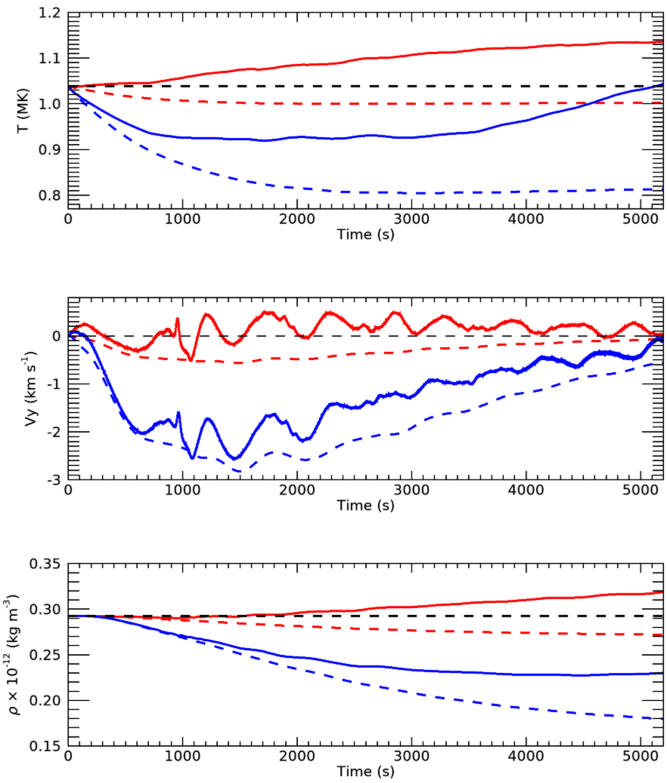

Figure 4. Top: Evolution of the temperature at the apex of the loop in the shell region ($y = -1.4$Mm). Middle: v_y, integrated over the 1st TR-coronal boundary in the left-hand shell region as a function of time. Bottom: Repeat of the top panel, but for the density.

3 RESULTS

3.1 Reduced Background Heating

Starting from the equilibrium state described in Section 2, the background heating is reduced to 90% and 50% of the original value, at the same time as the driving force is applied (i.e. as when Alfvén waves begin propagating along the loop). The (original) reference simulation, where the full (100%) background heating is applied, is discussed in detail in Section 3.1 of Callingham et al. (2024), where it is referred to as the viscous P= 10s driven simulation. The upper panel of Figure 5 shows the maximum of v_z in the shell region for the $\mathrm{Sim}_{90\ \%}$ and $\mathrm{Sim}_{50\ \%}$ driven cases, as well as the reference $\mathrm{Sim}_{100\ \%}$ simulation. Initially, the amplitudes are similar, and they increase in all three simulations at 700s when the chromospheric reflection interacts with the driven region. After this initial increase, the maximum amplitudes diverge, remaining roughly constant in the $\mathrm{Sim}_{100\ \%}$ and $\mathrm{Sim}_{90\ \%}$ cases and increasing in the $\mathrm{Sim}_{50\ \%}$ case. In the $\mathrm{Sim}_{50\ \%}$ case, the reduced heating creates downflows, moving mass from the corona into the TR; after 5200s, the driven region density increases by 15% at the outer edge of the shell region (at $x = -1.4$ Mm, see lower panel of Figure 5), increasing the driving force which is proportional to the density (Eq. 3). Due to the larger initial mass in the interior, the density in the driven region increases by more than a factor of 2, resulting in a driving force more than twice as large. However, since there is no phase mixing and thus little to no dissipation within the interior, this has a negligible impact on the simulation. Although this effect will also occur in the $\mathrm{Sim}_{90\ \%}$ simulation, the mass drain is insufficient (less than 5%) to significantly affect the driver, and thus the amplitude of v_z remains approximately constant.

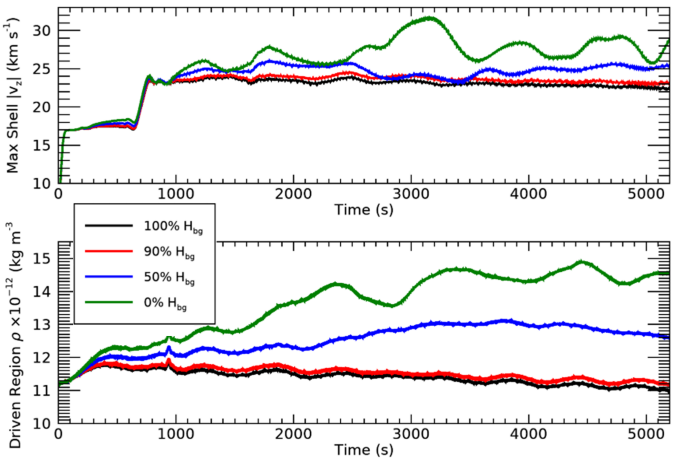

Figure 5. Upper: Plot of the maximum of $|v_z|$ in the shell region for the 100 % (black), $\mathrm{Sim}_{90\ \%}$ (red), $\mathrm{Sim}_{50\ \%}$ (blue) and 0 % (green) simulations. The shell region is defined as between ($-1.4\mathrm{Mm} < x < -0.6\mathrm{Mm}$). Lower: Plot of the density inside the driven shell region at the edge of the shell region ($x = -1.4\mathrm{Mm}$, $y = 10\mathrm{Mm}$).

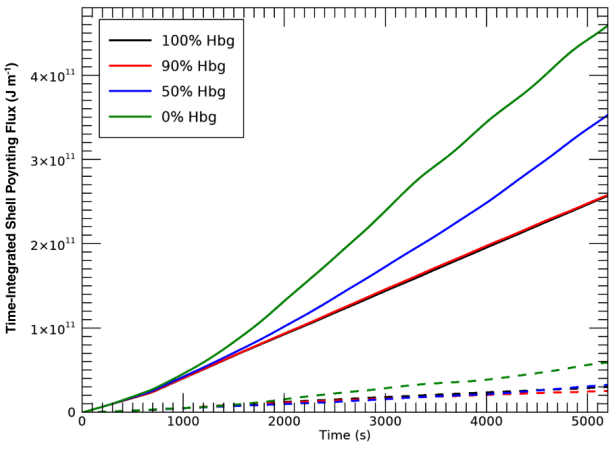

Figure 6. Plot of the time-integrated Poynting flux, where S is the TR-coronal boundary inside the left shell region: $\int_0^t \int_S [E \times B]_y$ dSdt. The solid lines represent the Poynting flux passing through the 1st TR-coronal boundary, and the dashed lines the 2nd TR-coronal boundary.

To quantify the amount of energy dissipated inside the coronal domain, we consider the difference in the Poynting flux passing through the 1st (solid) and 2nd (dashed) TR-coronal boundaries, $[\mathrm{PF}]_y = \int_0^t \int_S [E \times B]_y dSdt$, shown in Figure 6. Only the y-component of the flux is considered, as it is the dominant component for transverse Alfvénic perturbations. The difference between the solid and dashed lines can be considered analogous to the amount of flux dissipated within the corona. As expected, the Poynting flux injected into the corona is highest in the $\mathrm{Sim}_{50\ \%}$ simulation due to the larger amplitude waves propagating within the corona. The stronger driving force, caused by the increased density in the driven region, leads to the injection of a third more flux into the corona by the end of the simulation, compared to the $\mathrm{Sim}_{100\ \%}$ and $\mathrm{Sim}_{90\ \%}$ cases, which inject an almost identical amount. At all times in all three of the simulations, over $\mathrm{Sim}_{90\ \%}$ of the flux is dissipated within the corona, implying that highly efficient phase mixing occurs within the shell region. Hence, the rate of dissipation is relatively unaffected by reducing the background heating function; i.e., the phase mixing process remains unchanged due to the changes in the coronal plasma that occur with the reduction of the background heating function, as the density gradient is relatively unchanged.

Viscous dissipation of the Poynting flux inside the shell regions acts as a source of energy, counterbalancing some proportion of the energetic losses. In the $\mathrm{Sim}_{90\ \%}$ case, the dissipated wave energy is sufficient to completely counterbalance the energetic losses and generate moderate heating within the shell region. The upper panel of Figure 4 shows the evolution of temperature as a function of time at a single point within the loop apex inside the shell region ($x = -1.4\mathrm{Mm}$, $y = 60\mathrm{Mm}$). At early times in the simulation, wave heating can instantly offset the small decrease in the background heating function, before moderate heating occurs after 1000s, increasing the apex shell temperature by 0.1MK compared to the initial state by the end of the simulation. The heating is sufficient to prevent significant downflows from occurring when the background heating is reduced within the shell region. After 2000s, the field-aligned flows remain positive for the rest of the simulation, driving a small increase in coronal shell density, before tending towards zero as the system approaches a new equilibrium at t=5200s. Both the temperature and density continue to increase gradually, as the plasma begins to equilibrate between the increased energetic losses and continually dissipated wave energy. At the end of the simulations, at the outer edge of the shell region, the coronal shell temperature has increased by 8 – 14% and the density by 5 – 9% (Figure 7). Thus, the dissipated wave energy is sufficient to generate and maintain a new, hotter and denser equilibrium in the shell, despite the small reduction in the size of the background heating function. This indicates that the energy dissipated in the corona exceeds the effective energy loss due to the reduction in the background heating profile in the shell region.

Wave heating within the shell region provides sufficient thermodynamic feedback to broaden the initial transverse density profile, thereby expanding the shell outward toward the exterior. The mass change in the shell region increases the size of the cross-field density gradients towards the exterior, expanding the region where efficient phase mixing can occur. The right-hand panel of Figure 3 shows the cross-field Alfvén speed gradient at the loop apex. After 5200s, the density profile has altered sufficiently to create a notable Alfvén speed gradient across most of the exterior. The shell expands towards the exterior rather than the interior, as the plasma in the interior region has a higher thermal capacity and associated energetic losses, making it more difficult to heat. In addition, the density of the driven region in the interior is smaller than that of the shell and exterior; therefore, the driving force and amplitude of the driven waves are also smaller. At the centre of the shell, the Alfvén speed gradient decreases as the density difference between the interior and exterior decreases, thereby reducing the efficiency of phase mixing. However, dissipation remains highly efficient; thus, the dissipation and wave-heating processes within the shell region are relatively unaffected. The initially imposed transverse density profile is permanently broadened by wave heating, both increasing the efficiency of initially weaker phase mixing at the shell's outer edge and expanding the region where notable phase mixing and heating can occur.

In the $\mathrm{Sim}_{50\ \%}$ case, the dissipated wave energy cannot compensate for the larger decrease in background heating. Strong downflows of over 2 km s^{-1} occur, reducing the apex shell density by 20% after

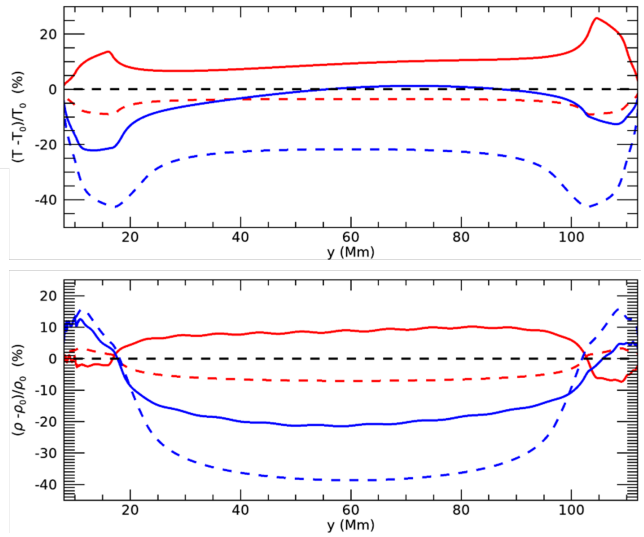

Figure 7. Plot of the change in temperature (upper) and density (lower) along the loop after 5200s, inside the shell region ($x = -1.4$Mm) for the driven (solid lines) and non-driven (dashed lines) $\mathrm{Sim}_{90\ \%}$ and $\mathrm{Sim}_{50\ \%}$ cases.

2000s (Figure 4). The temperature also decreases sharply, by 0.1MK, after the first 1000s. After this time, the temperature stabilises before gradually increasing. Reduced density and temperature decrease OTR and thermal conduction, thereby reducing the energy required to support the coronal plasma. The decreasing density also reduces the plasma's thermal capacity, thereby increasing the effectiveness of the dissipated wave energy in heating the plasma. The system becomes a complex balance as the amount of wave energy, the magnitude of energy losses, and the plasma's thermal capacity all change over time. The dissipated wave energy reduces the size of the chromospheric downflows, which cease completely by the end of the simulation. After the density begins to stabilise at 3500s, a large temperature increase occurs as the dissipated wave energy efficiently heats the less dense plasma and maintains the temperature against the now-reduced energetic losses.

Similarly to the $\mathrm{Sim}_{90\ \%}$ case, the thermodynamic feedback in the $\mathrm{Sim}_{50\ \%}$ simulation is sufficient to alter the cross-field loop structure. The shell broadening is greater in the $\mathrm{Sim}_{50\ \%}$ case, as the less dense plasma is more easily heated. In addition, the comparatively larger increase in the TR mass (lower panel of Figure 5) further enhances the driving force, increasing the amount of wave energy injected into the corona. The heating is sufficiently strong to increase the temperature at the centre of the shell to a value greater than the reduced interior temperature (solid blue line in the left panel of Figure 3).

In both the $\mathrm{Sim}_{50\ \%}$ and $\mathrm{Sim}_{90\ \%}$ cases, small temperature and density asymmetries occur along the loop; Figure 7 shows the percentage change in temperature and density along the loop at the outer edge of the initial shell region ($x = -1.4$Mm). After 5200s, the temperature in the $\mathrm{Sim}_{90\ \%}$ simulation increases by almost twice as much in the second half of the loop compared to the first half (6.8% at $y = 25$Mm compared to 11.7% at $y = 95$Mm). At the outer edge of the shell, there is a comparatively modest Alfvén speed gradient, leading to most of the wave energy being dissipated in the second half of the loop. In the centre of the shell, where phase mixing is the most efficient, the majority of the flux is dissipated in the first half of the loop, resulting in a comparatively higher temperature and density in the first half of the loop. Hence, the size and direction of the asymmetries differ depending on the efficiency of the localised dissipation. In the $\mathrm{Sim}_{50\ \%}$ case, at early times when wave heating cannot fully balance the radiative losses, any dissipated wave energy is only able to reduce the size of the downflows and rate of temperature decrease.

3.2 No Background Heating

The simulations presented in Section 3.1 demonstrate that the presence of Alfvén wave heating can partially compensate for a reduction in the size of the background heating function. To investigate the impact of further reducing the background heating, an additional simulation was run in which the heating function was turned off (i.e., α was set to zero), henceforth referred to as the $\mathrm{Sim}_{0\ \%}$ case. In this case, temperature and density will collapse to zero in the absence of the background heating function; however, the timescale for this to occur is longer than the simulation runtime. As the density and temperature rapidly decrease, the reduction in energetic losses and thermal capacity of the plasma will likely be a more significant factor in the $\mathrm{Sim}_{0\ \%}$ simulation, leading to the most efficient wave heating.

The v_z waves generated in the $\mathrm{Sim}_{0\ \%}$ simulation behave similarly to the $\mathrm{Sim}_{90\ \%}$ and $\mathrm{Sim}_{50\ \%}$ cases; the size of the maximum amplitude is still determined by the interaction between the driven and reflected wave from the chromosphere at ≈ 700s. However, the removal of the background heating profile generates a large decrease in the coronal mass, subsequently increasing the mass of the driven region in the shell by 30% (lower panel of Figure 5). The mass change is sufficient to affect the propagation of the Alfvén waves, altering the nature of the interference between the driven region and the reflected waves from the chromosphere. Hence, the maximum amplitude in the corona becomes highly dynamic as the simulation evolves, as the continual mass decrease alters both the size of the driving force and the nature of the interference. The amplitude of v_z peaks at 3100s and is always larger than in the reduced background heating simulations (upper panel Figure 5). Thus, the amount of Poynting flux injected into the corona also increases; compared to the reference 100% simulation, the $\mathrm{Sim}_{0\ \%}$ case drives 75% more Poynting flux into the coronal shell region (Figure 6). The majority of the Poynting flux is dissipated within the corona throughout the simulation (over 85%), indicating that the phase mixing process is relatively unaffected by the collapsing coronal loop density structure. Hence, significantly more flux is dissipated within the corona in the $\mathrm{Sim}_{0\ \%}$ simulation compared to the reduced background heating case, and the amount of dissipated available wave energy increases as the simulation evolves.

Figures 8 and 9 show the cross-field and field-aligned temperature and density profiles at four different times, respectively. Initially, the temperature of the entire corona decreases rapidly, generating strong downflows of up to 5km s^{-1} within the shell region (green line in the middle panel of Figure 10). After 1300s, the density has decreased sufficiently for the dissipated wave energy to balance the remaining energetic losses in the centre of the shell, leading to a stabilisation in the coronal temperature. However, the evaporative upflows triggered by the initial temperature decrease throughout the entire simulation; consequently, the coronal density continually decreases. As the density decreases, the associated energetic losses and thermal capacity of the plasma also decrease, leading to only a small amount of reheating in the shell region. The shell apex temperature gradually increases, reaching 0.95MK at the end of the simulation (Figure 8). In the interior region, little to no wave dissipation occurs, leading to a faster rate of decrease in temperature and density.

After 1300s, the shell temperature, supported by the dissipation of wave energy, overtakes the interior temperature. Similarly, towards the end of the simulation, the shell density overtakes the interior

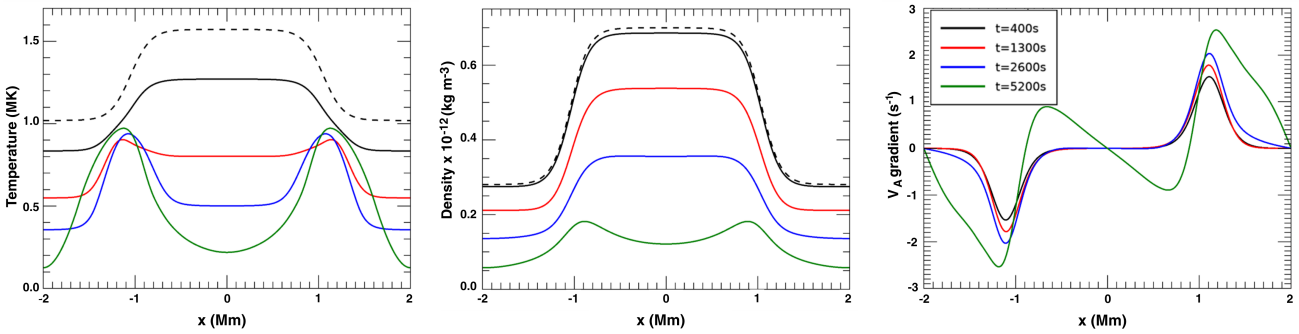

Figure 8. Plot of the temperature (left), density (middle) and cross-field Aflvén speed gradient (right) at the loop apex, at 4 different times in the $\mathrm{Sim}_{0\ \%}$ simulation. The black dashed line represents the initial equilibrium state.

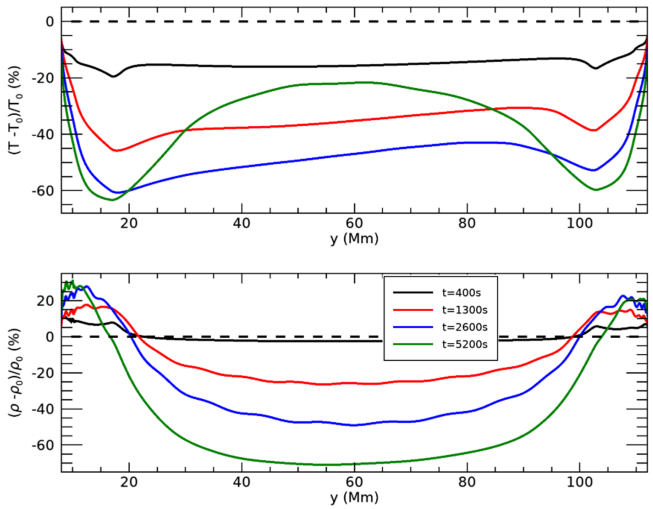

Figure 9. Plot of the change in temperature (upper) and density (lower) at 4 different times inside the shell region ($x = -1.4$Mm) for $\mathrm{Sim}_{0\ \%}$ simulation.

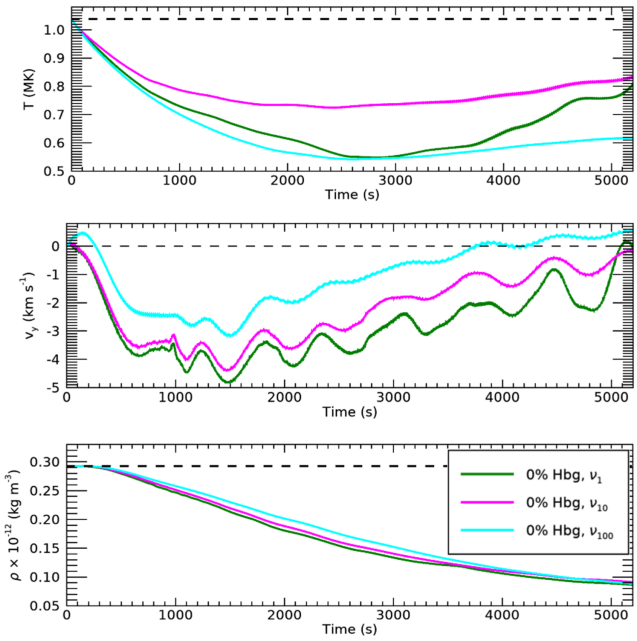

Figure 10. Top: Evolution of the temperature at the apex of the loop in the shell region ($y = -1.4$Mm). Middle: v_y, integrated over the 1st TR-coronal boundary in the left-hand shell region as a function of time. Bottom: Repeat of the top panel, but for the density.

density, significantly altering the initially imposed cross-field Alfvén speed gradient (right panel of Figure 8). The loop transitions from a smooth cross-section with a single peak to a 2-peak or two-strand structure, drastically altering the locations of Alfvén speed gradients and thus where phase mixing can occur. At the end of the simulation, Alfvén speed gradients exceeding $0.5\mathrm{s}^{-1}$ are present across almost the entire loop apex, indicating that efficient wave dissipation can occur throughout the loop.

As in the reduced background-heating simulations, temperature and density asymmetries occur along the loop in the $\mathrm{Sim}_{0\ \%}$ simulation. After 1300s and 2600s, the temperature and density are higher in the second half of the loop (Figure 9). The asymmetries are initially caused by localised wave dissipation: at the outer edge of the initial shell region, most dissipation occurs in the 2nd half of the loop. However, as the cross-field Alfvén gradient profile evolves, the efficiency of phase mixing increases at the shell edge, thereby shifting the localised heating towards the loop apex. This causes the temperature and density asymmetry to decrease over time.

4 DISCUSSION AND CONCLUSIONS

In this paper, a 2.5D atmospheric model of a coronal loop is presented, similar to the model described in Callingham et al. (2024). The loop consists of an isothermal chromosphere acting as a mass reservoir (Cargill et al. 2015), an artificially broadened TR (Lionello et al. 2009; Mikić et al. 2013) and a corona. To create a cross-field Alfvén speed profile, i.e., a shell region where phase mixing can occur, a transverse background heating profile is imposed. The background heating function is then reduced or removed, and a high frequency Alfvén wave driver is activated to drive Alfvén waves into the corona continually.

The simulations presented in Section 3.1 indicate that the phase mixing of Alfvén waves can act as a sufficient source of energy to compensate for a small reduction in the background heating profile. In the $\mathrm{Sim}_{90\ \%}$ case, the shell coronal temperature and density increased compared to the initial state. Furthermore, the cross-field

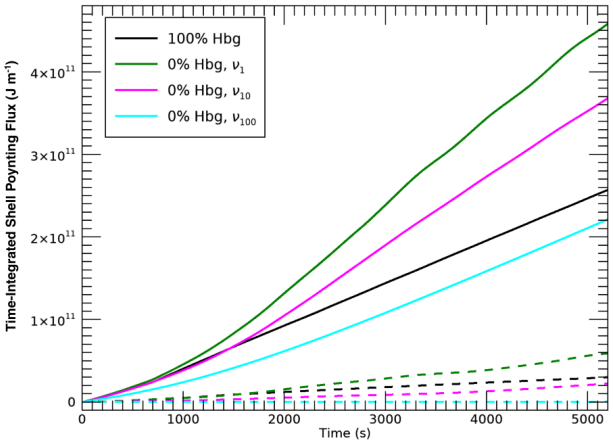

Figure 11. Plot of the time-integrated Poynting flux, where S is the TR-coronal boundary inside the left shell region: $\int_0^t \int_S [E \times B]_y$ dSdt. The solid lines represent the Poynting flux passing through the 1st TR-coronal boundary, and the dashed lines the 2nd TR-coronal boundary.

Alfvén speed gradient also increased within the exterior region, expanding the region where phase mixing and, thus, heating can occur. However, because the heating is localised to regions where phase mixing can occur, i.e., where a density gradient is present, the decreases in interior density and temperature are unaffected by the presence of the Alfvén waves.

In the $\mathrm{Sim}_{50\ \%}$ simulation, the effective energy loss is too significant for Alfvén wave dissipation to compensate, resulting in large downflows and reduced coronal density across the loop. However, the downflows increase the density within the driven region and hence, the driving force applied to the system, thereby increasing the amount of energy injected into the system. Moreover, the reduced density also decreases the OTR and thermal capacity of the plasma. Combining reduced energy losses with increased available wave energy generates heat within the shell, rapidly raising its temperature. In the end, wave heating in this setup can maintain a less-dense plasma at a temperature comparable to the initial loop profile. Similarly to the $\mathrm{Sim}_{90\ \%}$ case, wave heating can only act as an efficient energy source where density gradients are present. Thus, the interior density and temperature are reduced by nearly $\mathrm{Sim}_{50\ \%}$, resulting in a larger shell temperature at the apex than the interior temperature.

Section 3.2 investigated the consequences of fully removing the background heating profile, resulting in a near total collapse of the initial coronal density and temperature structure. The rapid reduction in density creates conditions for efficient wave heating within the shell region, allowing the coronal shell to reheat to near its initial temperature. However, the heating is constrained to the shell, as viscous heating in the absence of phase mixing is too slow compared to the cooling timescales of the corona. Hence, the interior loop structure will inevitably collapse when the artificial heating function is removed. This, combined with the efficient heating in the shells, leads to the evolution of the single loop into a 2-strand structure. It should be noted that the increase in the driver acceleration, caused by the mass draining from the corona from the loop collapse, is artificial, and a result of the choice of fixing the driving acceleration instead of the driving force. However, even in this augmented heating scenario, the waves cannot supply sufficient power to the corona to prevent the loop collapse.

To explore whether increasing the viscosity can broaden the region where heating occurs, two additional simulations were run with the kinematic viscosity value increased by a factor of ten and one hundred, referred to as the 10ν and 100ν simulations, and shown by the pink and teal lines in Figures 10, 11 and 12. The use of a higher-than-physical viscosity is often employed in other Lare studies (see e.g. Howson et al. 2019; Van Damme et al. 2020; Reid et al. 2023), as the higher value mitigates the computational limitation of simulating the small length scales characteristic of the solar corona. Increasing the viscosity strength should broaden the region where wave dissipation occurs efficiently, potentially increasing the lifespan of the initial cross-field density structure. However, it should be noted that the viscosity values in the 10ν and 100ν simulations are likely too high to be representative of a coronal loop; instead, these simulations are presented as a hypothetical, extreme dissipative scenario that maximises the heating extracted from waves.

The amplitude of the driven waves and thus the amount of flux injected into the corona decreases as the viscosity increases (Figure 11); the flux injected into the coronal shell region is 22% and 52% smaller after 5200s in the 10ν and 100ν simulations, respectively, compared to the $\mathrm{Sim}_{0\ \%}$ simulation discussed in Section 3.2 (henceforth referred to as the 1ν case). The amount of flux reduces due to the increased damping in the chromosphere, as the amplitude of the wave that interacts with the driven region is drastically reduced by the increased viscosity, as well as the additional damping that occurs as the waves propagate from the driven region into the corona. In the 100ν case, the wave is fully damped before re-propagating into the driven region, and thus no interference occurs. It should be noted that, as the point in the chromosphere where the reflection occurs is dependent on the numerical resolution, the process of amplitude increase via interaction between the reflected wave and driver is inherently artificial. Hence, the large decrease in available energy that occurs with increased viscosity is also artificial. However, it is reasonable to assume that in a coronal loop with stronger viscous forces, the amplitude of the Alfvén waves present in that loop would also be lower.

Due to the lower average amplitude of the Alfvén waves, the amount of flux injected into the corona decreases as the size of the viscosity increases (Figure 11). Within the shell, dissipation remains high; however, in the interior and exterior region, the dissipation rate rises from $\approx 20\%$ in the 1ν simulation to over $\approx 65\%$ and 100% in the 10ν and 100ν simulations. Hence, as efficient dissipation occurs outside the shell region, in the 100ν case, phase mixing is not the dominant dissipation mechanism. Figure 13 displays contour plots of the field-aligned and cross-field Alfvén speed gradients for the 1ν simulations after 1000s. The magnitude of the cross-field and field-aligned components is comparable in the 100ν case, with strong gradients in the lower corona. As the damping force is also proportional to the density, almost all damping occurs within the TR and lower corona. Little to no phase mixing occurs in the 100ν simulations, allowing for near-uniform dissipation across the loop. In the 10ν case, the viscosity is strong enough to cause notable dissipation within the exterior and interior regions, but weak enough to allow phase mixing to occur and for the cross-field gradient to govern dissipation within the shell region.

The reduction in total flux injected decreases the apex shell temperature in the 10ν and 100ν simulations; however, sufficient flux is dissipated in the exterior and interior to support a higher temperature (Figure 10). Thus, in conjunction with the higher viscosity, which inhibits the initial downflows, the rate of mass decrease is also reduced

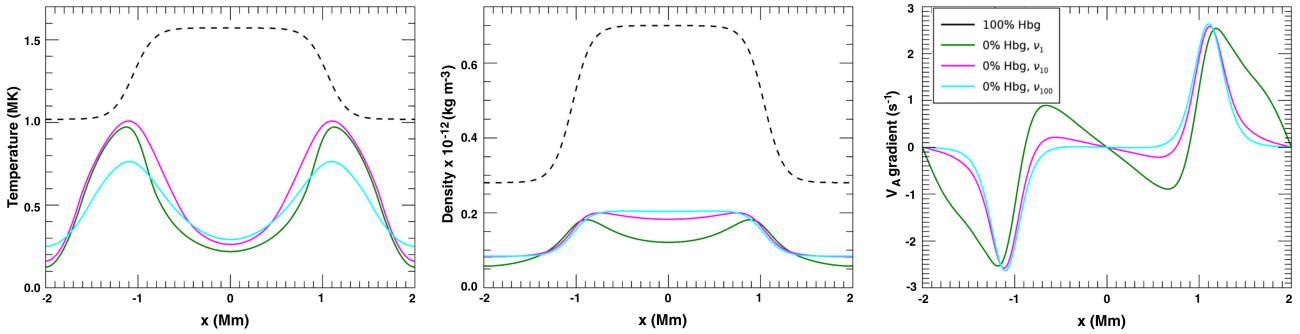

Figure 12. Plot of the temperature (left), density (middle) and cross-field Aflvén speed gradient (right) at the loop apex after 5200s, in the three viscous $\mathrm{Sim}_{0\ \%}$ cases. The black dashed line represents the initial equilibrium state.

in these regions. The relative decrease in interior temperature and density compared to the shell is insufficient for a two-peak density structure to appear in the 100ν simulation, resulting in the Alfvén speed gradient remaining localised to the initial shell region. At the end of the 10ν simulation, density gradients begin to appear within the interior region, implying that a similar structure to that seen in the 1ν case would emerge at a later time. In addition, in the 10ν case, the shell temperature stabilises considerably faster than the 1ν simulation, and at a notably higher temperature. After 1800s, the temperature remains at 0.8MK, compared to only $\approx$ 0.57MK after 2600s. However, both simulations approach a similar final temperature because the 're-heating' in the 1ν simulation is larger.

In conclusion, Alfvén wave heating has been shown to partially offset the reduction or removal of the artificial background heating profile. In the case of a small decrease in the heating function, wave heating in the shell region offset the reduction, resulting in moderate heating and a mass increase in the corona. Moreover, similarly to the conclusions of Callingham et al. (2024), the heated region expanded towards the exterior, broadening the shell region and thus the region where efficient phase mixing and dissipation can occur. When the background heating function was fully removed, wave heating could not prevent the loop density from nearly collapsing. The system became a complex interplay among increased available energy, reduced energetic losses, and decreased thermal capacity of the plasma. Shell heating is sufficient to slow the decrease in density, causing the shell density to overtake the interior density and create a two-peak cross-field density profile. In the higher-viscosity simulations, heating can occur across the loop profile, since phase mixing is not required to achieve efficient heating; however, the increased viscosity significantly reduces the flux injected into the corona and may inhibit the formation of small-scale structures via phase mixing.

ACKNOWLEDGEMENTS

H.C. acknowledges financial support by the UK's Science and Technology Facilities Council (STFC) Doctoral Training Partnership Grant ST/V507076/1 and the Royal Society Wolfson Fellowship (RSWF/FT/180005). IDM received funding from the Research Council of Norway through its Centres of Excellence scheme, project number 262622. We acknowledge support from the ASI/INAF agreement n. 2022-29-HH.0.

DATA AVAILABILITY

The data from the numerical simulations and analysis presented in this paper are available from the corresponding author upon reasonable request.

REFERENCES

Alfvén H., 1942, Nature, 150, 405
Antolin P., Okamoto T. J., De Pontieu B., Uitenbroek H., Van Doorsselaere T., Yokoyama T., 2015, The Astrophysical Journal, 809, 72
Arregui I., 2015, Philosophical Transactions of the Royal Society A: Mathematical, Physical and Engineering Sciences, 373, 20140261
Berghmans D., de Bruyne P., 1995, Astrophysical Journal v. 453, p. 495, 453, 495
Bradshaw S. J., Cargill P. J., 2013, The Astrophysical Journal, 770, 12
Braginskii S., 1965, Reviews of plasma physics, 1, 205
Callingham H., De Moortel I., Pagano P., 2024, Monthly Notices of the Royal Astronomical Society, 535, 1640
Cargill P., Warren H., Bradshaw S., 2015, Philosophical Transactions of the Royal Society A: Mathematical, Physical and Engineering Sciences, 373, 20140260
Cargill P., De Moortel I., Kiddie G., 2016, The Astrophysical Journal, 823, 31
De Moortel I., Nakariakov V. M., 2012, Philosophical Transactions of the Royal Society A: Mathematical, Physical and Engineering Sciences, 370, 3193
De Pontieu B., Martens P., Hudson H., 2001, The Astrophysical Journal, 558, 859
Heyvaerts J., Priest E. R., 1983, Astronomy and Astrophysics, vol. 117, no. 2, Jan. 1983, p. 220-234., 117, 220
Hinode Review Team K., et al., 2019, Publications of the Astronomical Society of Japan, 71, R1
Hollweg J. V., 1984, Astrophysical Journal, Part 1 (ISSN 0004-637X), vol. 277, Feb. 1, 1984, p. 392-403. Research supported by the Science and Engineering Research Council of England., 277, 392
Howson T. A., De Moortel I., 2022, Astronomy & Astrophysics, 661, A144
Howson T., De Moortel I., Reid J., Hood A., 2019, Astronomy & Astrophysics, 629, A60
Jess D. B., et al., 2016, Nature Physics, 12, 179
Klimchuk J. A., 2015, Philosophical Transactions of the Royal Society A: Mathematical, Physical and Engineering Sciences, 373, 20140256
Klimchuk J., Patsourakos S., Cargill P., 2008, The Astrophysical Journal, 682, 1351
Lionello R., Linker J. A., Mikić Z., 2009, The Astrophysical Journal, 690, 902
McIntosh S. W., De Pontieu B., Carlsson M., Hansteen V., Boerner P., Goossens M., 2011, Nature, 475, 477

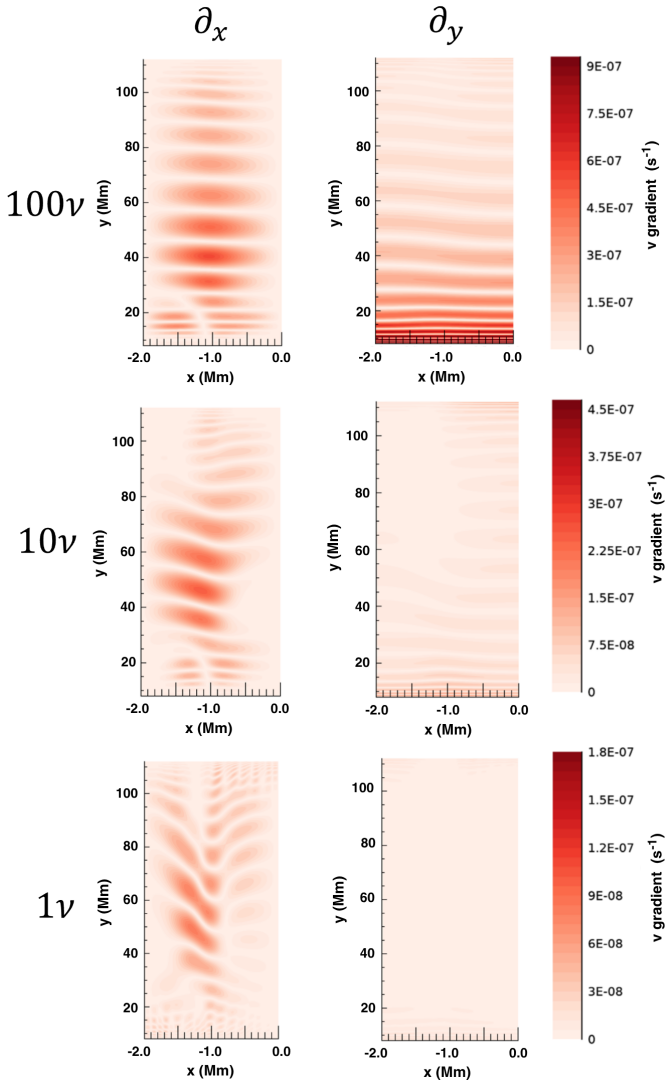

Figure 13. Contour plots of $\frac{\partial v_z}{\partial x}$ (left) and $\frac{\partial v_z}{\partial y}$ (right) at t=1000s, for the 100ν (top), 10ν (middle) and 1ν (bottom) cases.

McMurdo M., Ballai I., Verth G., Alharbi A., Fedun V., 2023, The Astrophysical Journal, 958, 81
Mikić Z., Lionello R., Mok Y., Linker J. A., Winebarger A. R., 2013, The Astrophysical Journal, 773, 94
Ofman L., Klimchuk J., Davila J., 1998, The Astrophysical Journal, 493, 474
Okamoto T. J., Antolin P., De Pontieu B., Uitenbroek H., Van Doorsselaere T., Yokoyama T., 2015, The Astrophysical Journal, 809, 71
Pagano P., De Moortel I., 2017, Astronomy & Astrophysics, 601, A107
Pagano P., De Moortel I., 2019, Astronomy & Astrophysics, 623, A37
Parnell C. E., De Moortel I., 2012, Philosophical Transactions of the Royal Society A: Mathematical, Physical and Engineering Sciences, 370, 3217
Pelouze G., Van Doorsselaere T., Karampelas K., Riedl J. M., Duckenfield T., 2023, Astronomy & Astrophysics, 672, A105
Prokopyszyn A., Hood A., De Moortel I., 2019, Astronomy & Astrophysics, 624, A90
Reid J., Threlfall J., Hood A. W., 2023, Monthly Notices of the Royal Astronomical Society, 518, 1584
Rosner R., Tucker W. H., Vaiana G., 1978, Astrophysical Journal, Part 1, vol. 220, Mar. 1, 1978, p. 643-645, 647, 649-653, 655-665. Research supported by the Smithsonian Institution;, 220, 643
Srivastava A. K., et al., 2021, Chromospheric heating by magnetohydrodynamic waves and instabilities
Van Damme H., De Moortel I., Pagano P., Johnston C. D., 2020, Astronomy & Astrophysics, 635, A174
Van Doorsselaere T., et al., 2020, Space Science Reviews, 216, 1
Weberg M. J., Morton R. J., McLaughlin J. A., 2018, The Astrophysical Journal, 852, 57
Wentzel D. G., 1974, Solar Physics, 39, 129
Zhou Y.-H., Ruan W.-Z., Xia C., Keppens R., 2021, Astronomy & Astrophysics, 648, A29

This paper has been typeset from a TEX/LATEX file prepared by the author.